LASER & PHOTONICS REVIEWS
www.lpr-journal.org

Maximized Enhancement of Polarized and Unpolarized Emissions via Critical Coupling in Brillouin Zone Folding Metasurfaces

*Jungho Han, Yeonsoo Lim, Jeheon Lee, Seongheon Kim, and Young Chul Jun**

Critical coupling can induce maximized field enhancement in resonant optical modes. Therefore, it is important for various photonic technologies. Here, it is shown that directional light sources with highly enhanced emission intensities can be realized via critical coupling. A clear experimental demonstration of maximized emission enhancement is presented in quantum dot (QD)-coated Brillouin zone folding (BZF) metasurfaces. BZF dielectric metasurfaces support guided-mode resonances, where the radiative quality factor can be gradually tuned by structural parameters, allowing critical coupling to occur at the QD emission wavelength. Maximized enhancements of polarized and unpolarized emissions are demonstrated in the normal direction, resulting in highly enhanced, directional, and narrow-angled emissions. The investigations indicate that light emission from quantum emitters can be optimized via critical coupling and that BZF metasurfaces can provide a highly tunable platform for both polarization-sensitive and polarization-insensitive critical coupling. Maximized field enhancement and highly enhanced light–matter interactions in BZF metasurfaces are important for a wide range of photonic technologies such as light sources, photodetectors, sensors, nonlinear enhancement, and quantum photonic devices.

1. Introduction

Critical coupling allows the maximal delivery of incident optical energy into photonic structures; therefore, it can be exploited in various photonic technologies.[1–11] Critical coupling into a resonant optical mode occurs when the radiative and nonradiative quality (Q) factors of the optical mode are equal. Optical field enhancement in the optical mode is also maximized at the critical coupling condition.[12,13] The strongly enhanced field intensity in resonant photonic structures can lead to significant enhancements in various types of light–matter interactions.

J. Han, Y. Lim, J. Lee, S. Kim, Y. C. Jun
Department of Materials Science and Engineering
Ulsan National Institute of Science and Technology (UNIST)
Ulsan 44919, Republic of Korea
E-mail: ycjun@unist.ac.kr
Y. C. Jun
Graduate School of Semiconductor Materials and Devices Engineering
UNIST
Ulsan 44919, Republic of Korea

The ORCID identification number(s) for the author(s) of this article can be found under https://doi.org/10.1002/lpor.202401923

DOI: 10.1002/lpor.202401923

Dielectric metasurfaces, which are planar dielectric pattern arrays with subwavelength structures, have recently been employed as general platforms in various nanophotonic studies. Light emission from the emitters combined with metasurfaces can be significantly enhanced because of high-Q optical resonances in dielectric metasurfaces.[14–22] Moreover, the direct control of emission fields and emission characteristics can be achieved using dielectric metasurfaces, including the control of emission polarization, directionality, and wavefronts, leading to enhanced functionalities for compact light sources.[23–30]

In this study, we show that emission enhancement can be maximized using critical coupling. According to the Lorentz reciprocity principle, the far-field emission enhancement of light emitters can be obtained by integrating the field intensity in a light-emitting medium under incident light.[14,31,32] Consequently, maximized emission enhancement can be achieved at the critical coupling condition owing to the maximized field intensity. We present a clear experimental demonstration of maximized emission enhancement via critical coupling. Generally, it is challenging in practice to exactly match the radiative and nonradiative Q factors and achieve maximized enhancement. Here, Brillouin zone folding (BZF) metasurfaces are employed to address this issue. Specifically, we demonstrate the maximized enhancement of polarized and unpolarized emissions from semiconductor quantum emitters using polarization-sensitive and polarization-insensitive critical coupling in BZF metasurfaces. Recently, BZF has emerged as a novel method in metasurface design.[33–44] New high-Q modes with unique optical properties and enhanced light–matter interactions can be obtained in dielectric metasurfaces by controlling the lattice symmetry. For example, symmetry breaking via period-doubling perturbation allows guided modes, which originally lie below the light line and are forbidden from leaking out, to be folded into the continuum. This BZF can lead to the emergence of high-Q optical resonances such as BZF-induced guided mode resonances (GMRs) and quasi-bound states in the continuum (quasi-BICs).[38,41] Importantly, the radiative Q factor can be gradually tuned in both cases by adjusting the structural parameters (e.g., particle size or gap

distance in the particle pair). Therefore, BZF can be directly utilized to induce and tune critical coupling in metasurfaces. However, such critical coupling in BZF metasurfaces has not been systematically studied or exploited.

Here, we consider dielectric (TiO_2) metasurfaces coated with semiconductor quantum dots (QDs) in the visible region. The QD layer exhibits small absorption losses at the emission wavelength. Polarization-sensitive or polarization-insensitive high-Q resonances appear in the normal direction when adjusting the lattice symmetry in a single direction (e.g., x-direction) only or in two directions. In this study, we use BZF-induced GMRs to gradually control the radiative Q factor and achieve critical coupling by balancing the radiative and nonradiative Q factors in QD-coated dielectric metasurfaces. Strong light confinement and field enhancement via GMRs result in highly enhanced light–matter interactions. The maximized field enhancement of incident light at the critical coupling condition leads to maximized emission enhancement by Lorentz reciprocity. In our experiments, we clearly demonstrate the maximized enhancement of polarized and unpolarized photoluminescence (PL) from CdSe/ZnS QDs coated on the surface of TiO_2 metasurfaces. Both the polarized and unpolarized emissions can be maximized in the normal direction by controlling the TiO_2 disk size, which results in highly enhanced, directional emission with a small divergence angle. In our study, while the absorption (excitation) enhancement at the excitation laser wavelength remains almost the same, the emission enhancement at the BZF-induced GMR wavelength is maximized via critical coupling. Polarization-sensitive critical coupling is achieved for the single-directional perturbation (x-direction only). Therefore, we obtain the maximized enhancement of polarized emission. For the bidirectional perturbation, critical coupling into a BZF-induced GMR is achieved for any incident polarization in the normal direction. Therefore, we obtain the maximized enhancement of unpolarized emission. This is directly confirmed by measuring the Stokes parameters of QD PL. Directional light sources of polarized and unpolarized light with highly enhanced emission intensities can be advantageous for advanced display technologies, such as augmented reality (AR).[45–48]

Our experimental demonstration clearly indicates that light emission from quantum emitters can be optimized via critical coupling and that BZF metasurfaces can provide a highly tunable platform for both polarization-sensitive and polarization-insensitive critical coupling. Critical coupling in BZF metasurfaces can be readily scaled to other frequency ranges such as the infrared and terahertz regions. Therefore, maximized field enhancement and the resulting strong light–matter interactions in BZF metasurfaces can be utilized in a wide range of photonic technologies such as light sources, photodetectors, sensors, nonlinear enhancement, and quantum photonics.

2. Results and Discussion

Figure 1a–d explain the band folding in our dielectric metasurface. The dielectric metasurface consists of a square array of TiO_2 disks coated with QDs on a transparent quartz substrate. The dimensions of the TiO_2 disk pattern are detailed in the caption of Figure 1. The disk size variation ΔD is defined as $\Delta D = D_0 - D$. We consider lattice symmetry breaking in two different ways: i) single-directional perturbation (along the x-direction only, as shown in Figure 1a) and ii) bidirectional perturbation (Figure 1c). In both cases, the size of one half of the disks is reduced (i.e., diatomic structure in the unit cell), and period doubling perturbation is introduced to reduce the size of the first Brillouin zone by half and, thus, induce GMRs at the gamma point. The previously inaccessible bound modes (guided modes) are folded above the light line of air, and the band edge modes at the boundary of the first Brillouin zone now lie at the gamma point and, therefore, are excitable by normally incident free-space light.

The band structures were obtained using the guided-mode expansion method.[49,50] The constant refractive indices are assumed for the TiO_2 and QD layers without absorption losses. Figure 1b,d show the corresponding band structures for single-directional perturbation (Γ-X direction) and bidirectional perturbation (Γ-M direction), respectively. The air and substrate light lines in the unperturbed metasurface are shown for reference. In the unperturbed metasurface without period-doubling perturbation (i.e., with identical disk sizes), all guided modes of interest at the Brillouin zone boundary reside below the light lines of the air and quartz substrates. Therefore, they represent bound modes that do not leak into the air or substrate. In addition, the unperturbed metasurface does not support GMRs at the gamma point in the wavelength region of interest. In both cases, band folding induces high-Q GMRs at the gamma point. The radiative Q factors of the GMRs were also obtained from the guided-mode expansion method (Figures S1–S3, Supporting Information). The single-directional perturbation induces GMRs at the gamma point with a Q factor of 446 (ΔD = 10 nm) and 233 (ΔD = 20 nm). The bidirectional perturbation induces both high-Q GMR and quasi-BIC at the gamma point that exhibits different k dependences on the Q factor (Figure S1d, Supporting Information).[38,41] The bidirectional perturbation induces two GMRs that are degenerate at the gamma point (e.g., ≈2.2 eV for ΔD = 20 nm). The two degenerate GMRs are odd and even modes with respect to the vertical (xz) mirror plane. The radiative Q factor of the quasi-BIC is significantly higher than that of the GMR, making the quasi-BIC difficult to use for critical coupling at the gamma point in our QD-coated metasurface. Therefore, in this study, the GMR mode induced by band folding is considered for radiative Q control and critical coupling.

To further examine the mode properties, we conducted reflectance spectrum simulations for several different disk size perturbations (ΔD = 0–30 nm) using rigorous coupled wave analysis (RCWA).[51] The simulated angle-resolved reflectance spectra with disk size variations are shown for both cases in Figures S4 and S5 (Supporting Information). The angle-resolved spectrum is expressed as a function of free-space light wavelength λ and the in-plane wavevector component $k_x/k_0 = \sin\theta$, where $k_0 = 2\pi/\lambda$ and θ is an incidence angle. We considered both the y-polarized (or s-polarized) and x-polarized (or p-polarized) incidences. The simulated reflectance spectra are in good agreement with the band structure simulations. The reflectance spectrum for the single-directional perturbation in Figure S4 (Supporting Information) shows the excitation of GMR modes along the k_x direction under y-polarized incidence only, thus creating a linearly polarized state at the gamma point. The bidirectional perturbation introduced the GMR and quasi-BIC modes under both y- and x-polarized incidences (Figure S5, Supporting Information). The

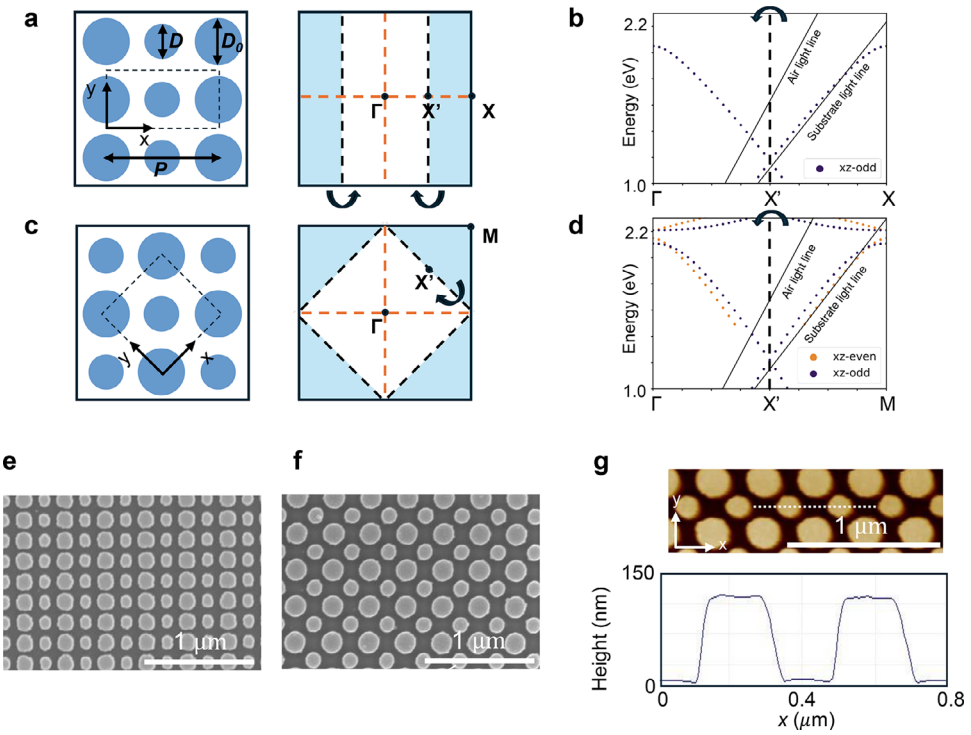

Figure 1. Brillouin zone folding (BZF) metasurfaces with single- and bidirectional lattice perturbations. a) Schematic for the period doubling perturbation in the x-direction and band folding (*P*: 380 nm, D_0: 150 nm, TiO_2 thickness: 120 nm). The disk size variation ΔD is defined as $\Delta D = D_0 - D$. The TiO_2 metasurface is covered by an additional 30 nm QD layer. b) The corresponding band structure obtained from the guided-mode expansion method (ΔD = 20 nm). The constant refractive indices of 2.27 and 1.51 are assumed for the TiO_2 and QD layers, respectively, without absorption losses. The air and substrate light lines in the unperturbed structure are shown for reference. c) Schematic for the bidirectional perturbation and band folding (*P*: 523 nm, D_0: 210 nm, TiO_2 thickness: 130 nm) and d) the corresponding band structure (ΔD = 20 nm). The two degenerate GMRs (≈2.2 eV) at the gamma point are odd and even modes with respect to the vertical (*xz*) mirror plane. e,f) SEM images of the bare TiO_2 metasurface for the single- and bidirectional perturbations, respectively. g) AFM height profile.

two degenerate GMR modes at the gamma point (indicated by the arrows) represent orthogonal polarization states and, therefore, create an unpolarized resonance in the normal direction. The reflectance spectra also show that the spectral linewidth of the GMR gradually increases with increasing perturbation (i.e., disk size variation ΔD). The radiative *Q* factor of the BZF-induced GMR gradually decreases with increasing perturbation; therefore, it is ideal for achieving critical coupling.

The TiO_2 dielectric metasurface was fabricated using electron beam lithography and etching (see the Experimental Section). Figure 1e,f show the scanning electron microscopy (SEM) images of the TiO_2 metasurface with single- and bidirectional perturbations, respectively. The height profile measured using atomic force microscopy confirms the formation of disk-shaped structures. For the QD PL measurements, the fabricated TiO_2 metasurface was coated with CdSe/ZnS QDs. Figure S6 (Supporting Information) shows the refractive indices of the TiO_2 and QD layers, which are measured using ellipsometry. The thickness (≈30 nm) of the QD layer was also determined from the ellipsometry measurement. Notably, the QD layer exhibits a small absorption loss at the emission wavelength. Figure S7 (Supporting Information) shows an SEM image of the BZF metasurface sample after QD coating and the PL image. The PL image confirms that the QD emission is almost uniform across the metasurface pattern. The angle-resolved reflectance spectra before and after QD coating were measured and compared, and the results are shown in Figure S8 (Supporting Information). When QDs were coated onto the sample, the resonance peak exhibited a spectral redshift; however, the overall features of the GMRs remained similar. The QD PL spectrum on a bare quartz substrate is shown in Figure S6c (Supporting Information) for reference.

Now, we consider the numerical simulations of field enhancement in the QD-coated BZF metasurface. We assumed a TiO_2 metasurface coated with a 30 nm thick QD layer (**Figure 2a**). We used the measured refractive indices of TiO_2 and QD layers in the simulations, including the absorption losses of the QD layer. PL enhancement has contributions from both the absorption (excitation) and emission enhancements. Figure S9 (Supporting Information) shows the simulated absorptance spectra in the single- and bidirectional perturbed metasurfaces near the laser excitation wavelength (450 nm) for several different perturbation ΔD's. In all cases, the absorptance remains almost the same. Therefore, in the proposed metasurface, we expect that the differences in PL enhancement are determined by the emission enhancement at the GMR wavelengths. Using Lorentz reciprocity, this emission enhancement can be studied by integrating the field intensity in the light-emitting QD layer under incident light.[14,31,32] The Lorentz reciprocity principle states that the source and detector of electromagnetic fields can be interchanged without affecting the physical situation.[52] Therefore, the far-field emission power

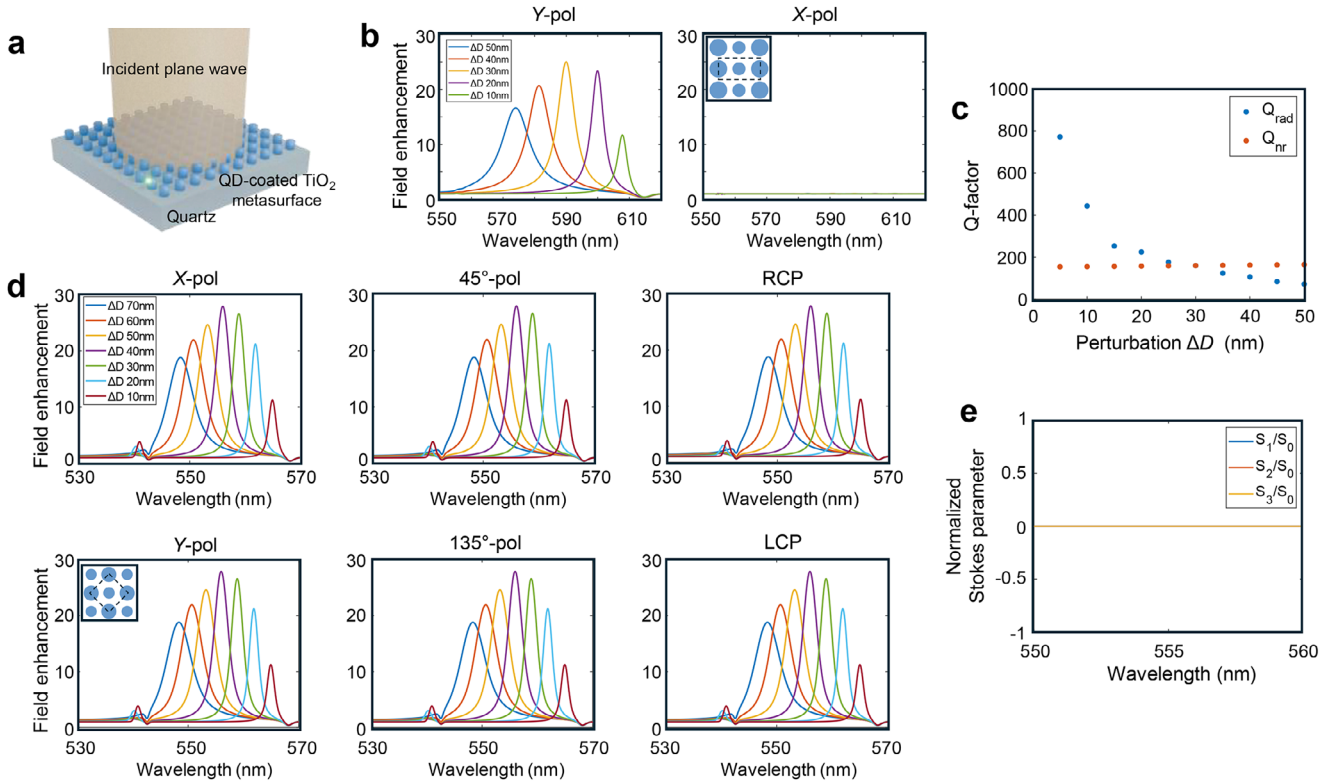

Figure 2. Field enhancement calculations in the QD layer. a) Schematic of the QD-coated dielectric metasurface. b) Simulated field enhancement spectra under normal incidence of light for the single-directional perturbation (ΔD = 10–50 nm). By reciprocity, these field enhancements correspond to the emission enhancement. The left and right panels show the cases for *y*- and *x*-polarized incident light, respectively. The measured refractive indices of TiO_2 and QD layers are used in the simulations, including the absorption losses of the QD layer. c) The radiative and nonradiative Q factors extracted from the simulated reflection spectra for different ΔD values (Figure S10, Supporting Information). d) Simulated field enhancement spectra in the normal direction for the bidirectional perturbation (ΔD = 10–70 nm). The enhancement spectra are shown for six incidence polarizations that determine the Stokes parameters. e) The normalized Stokes parameters for ΔD = 40 nm, obtained from the field enhancement simulations in d). This confirms the enhancement of unpolarized emission: $S_1/S_0 = S_2/S_0 = S_3/S_0 = 0$. Note that, becaue the metasurface with single-directional perturbation has smaller disk size and periods, the single-directional case has a larger effective perturbation for the same ΔD than the bidirectional case.

and polarization from an ensemble of randomly positioned and oriented dipolar emitters can be obtained by integrating the total field enhancements at the dipole positions under incident light. Compared with dipole simulations, field enhancement simulations in photonic structures simplify emission calculations and are more straightforward to understand and optimize.

For given material absorption losses, the maximum field enhancement can be reached by adjusting the disk size of the proposed BZF metasurface. The field enhancement factor I in a resonant optical mode can be obtained from the temporal coupled-mode theory as follows (see Note S1, Supporting Information for the derivation):

$$I \propto \frac{Q^2}{Q_{\mathrm{rad}}} \tag{1}$$

where $Q = \omega_0/2(\gamma_{\mathrm{rad}} + \gamma_{\mathrm{nr}})$ and $Q_{\mathrm{rad}} = \omega_0/2\gamma_{\mathrm{rad}}$ are the total and radiative Q factors, respectively; ω_0 is the resonance frequency; and γ_{rad} and γ_{nr} are the radiative and nonradiative damping rates, respectively. We find that the field enhancement in the resonant optical mode is determined by the balance between radiative and nonradiative Q factors. From $\mathrm{d}I/Q_{\mathrm{rad}} = 0$, we find that the emission enhancement reaches a maximum at $Q_{\mathrm{rad}} = Q_{\mathrm{nr}}$ (critical coupling). By Lorentz reciprocity, emission enhancement can be calculated by integrating the field intensity in the emitter layer under incident light. Therefore, the emission enhancement also reaches a maximum at the critical coupling condition.

BZF metasurfaces provide a general platform for both polarization-sensitive and polarization-insensitive critical coupling; Q_{rad} gradually decreases with increasing perturbation, whereas Q_{nr} due to absorption in the QD layer remains similar. Figure 2b shows the field enhancement calculation at each ΔD for the single-directional perturbation under the normal incidence of light (i.e., at the gamma point). The electric field intensity was integrated in the QD layer and normalized to the integrated field intensity at $\Delta D = 0$ to ease the comparison with the experimental results later. The *y*-polarized incident light induces a GMR mode in the BZF metasurface (Figure S4, Supporting Information), and the field enhancement initially increases with increasing perturbation ΔD and then reaches a maximum at ΔD = 30 nm. Subsequently, it decreases back with a further increase in perturbation. A field-enhancement peak appears in the GMR position at the gamma point. By stark contrast, for *x*-polarized

incident light, no enhancement peaks are observed in the normal direction.

To examine the critical coupling condition, the radiative and nonradiative Q factors (Q_{rad} and Q_{nr}) are also directly extracted from the simulated reflectance spectra, which exhibit asymmetric Fano-resonant spectral lineshapes (Figure S10, Supporting Information). The Q_{rad} and Q_{nr} were obtained by fitting the reflectance spectra to the Fano resonance equation (Equation S3 and Note S1, Supporting Information). Figure 2c shows the extracted radiative and nonradiative Q factors for different ΔD values. As ΔD increases, Q_{rad} gradually decreases, whereas the nonradiative Q factor due to the absorption in the QD layer remains almost the same. This plot directly confirms that critical coupling is achieved at $\Delta D = 30$ nm, leading to the maximized field enhancement at $\Delta D = 30$ nm, as shown in Figure 2b for y-polarized incident light. The wavelength of the maximum emission enhancement can be further tuned by adjusting structural parameters such as the pattern period.

The metasurface with single-directional perturbation supports another high-Q band along the Γ-Y direction (i.e., k_y direction) due to the band folding from the guided modes along the X-M direction (see the schematic and simulated reflectance spectra in Figure S11, Supporting Information).[53,54] The reciprocity calculation in Figure S12 (Supporting Information) shows the field enhancement (or emission enhancement) over the k_x-k_y plane for y- and x-polarized incidences ($\Delta D = 30$ nm). At the maximized enhancement wavelength (585.5 nm), the emission enhancement is significant only near the gamma point along the k_x direction while the enhancement is more extended along the k_y direction (for y-polarized incidence). As the wavelength changes, the enhancement along the k_x direction decreases rapidly while the enhancement along the k_y direction persists for shorter wavelengths at different k_y positions. This behavior agrees well with the emission enhancement spectra along the k_x and k_y directions (Figures S13 and S14, Supporting Information, respectively). We also notice that the emission enhancement is significant for y-polarized incidence, and thus the emission is strongly y-polarized for the single-directional perturbation. Although the x-polarized incidence has some features along the diagonal directions in the k_x-k_y plane, the enhancement is much weaker.

Similar field enhancement calculations were also conducted for the bidirectional perturbation that induces an unpolarized resonance in the normal direction. To confirm the enhancement of the unpolarized field, we conducted simulations for the six polarization components that determine the Stokes parameters: x- and y-polarizations, 45° and 135° linear polarizations, and right and left circular polarizations (RCP and LCP, respectively). Figure 2d shows the calculated field enhancement spectra for these six incident polarizations in the normal direction. In all cases, field enhancement exhibits the same behavior with increasing perturbation, and it reaches a maximum at $\Delta D = 40$ nm. Notably, the bidirectional perturbation induces GMR modes with higher radiative Q factors than the single-direction perturbation. Therefore, the BZF metasurface with the bidirectional perturbation requires a larger ΔD to balance with the nonradiative Q factor and achieve critical coupling.

By reciprocity, this polarization-insensitive field enhancement leads to an enhancement in the unpolarized emission in the normal direction. From the simulated six polarization components, the Stokes parameters of the emission are calculated for $\Delta D = 40$ nm (Figure 2e). The normalized Stokes parameters are obtained using Equations (2)–(4). The Stokes parameters (S_0, S_1, S_2, and S_3) fully characterize the polarization state of light: S_1/S_0 and S_2/S_0 describe a degree of linear polarization, whereas S_3/S_0 describes a degree of circular polarization. The total intensity S_0 is the sum of any two orthogonally polarized intensities.

$$S_1/S_0 = \left(I_0 - I_{90}\right) / \left(I_0 + I_{90}\right) \tag{2}$$

$$S_2/S_0 = \left(I_{45} - I_{135}\right) / \left(I_{45} + I_{135}\right) \tag{3}$$

$$S_3/S_0 = \left(I_{RCP} - I_{LCP}\right) / \left(I_{RCP} + I_{LCP}\right) \tag{4}$$

where I_0, I_{90}, I_{45}, I_{135}, I_{RCP}, and I_{LCP} are the intensities of the six polarization components, respectively. Figure 2e clearly shows the features of unpolarized emission: $S_1/S_0 = S_2/S_0 = S_3/S_0 = 0$. This confirms that the maximized enhancement of the unpolarized emission can be achieved by the BZF-induced GMR mode using the bidirectional perturbation.

The PL spectra of the QD-coated TiO_2 metasurface were measured using continuous-wave laser excitation at 450 nm in a custom-built Fourier plane measurement setup (Figure S15, Supporting Information). **Figure 3** shows the measured angle-resolved PL spectra along the k_x direction for the single-directional perturbation with varying disk sizes ($\Delta D = 0$–50 nm). In agreement with the simulations shown in Figure 2b, the y-polarized PL spectrum exhibits a strongly enhanced PL spot in the GMR position at the $k_x = 0$ point (i.e., in the normal direction), whereas the x-polarized PL spectrum does not exhibit such an emission enhancement feature. The maximized QD emission is indicated by the arrow in the angle-resolved PL spectrum (Figure 3a). Although the original QD emission on a bare substrate exhibits a spectrally broad emission at wide emission angles, the QD-coated metasurface exhibits intense and highly directional emission owing to optical coupling to the BZF-induced GMR mode.

Figure 3b shows the emission enhancement factor in the normal direction, obtained by normalizing to the PL spectrum at $\Delta D = 0$. Because the absorption enhancement at the excitation laser wavelength remains almost the same for all ΔD's (Figure S9, Supporting Information), the normalization of the experimental PL spectrum to that at $\Delta D = 0$ cancels out the contribution from the absorption enhancement; thus, emission enhancement factors can be obtained from the experimental PL measurement data. For the y-polarized PL, the emission enhancement initially increases with increasing perturbation ΔD and reaches a maximum (≈20 times) at $\Delta D = 30$ nm. Subsequently, it decreases with a further increase in perturbation. This experimental behavior is found to be in good agreement with the simulated field enhancements shown in Figure 2b. Moreover, the y-polarized experimental spectrum shows gradually increasing spectral linewidths with larger perturbations owing to the increased radiative damping of the GMR mode. Figure 3c shows the angular distribution of the QD emission ($\Delta D = 30$ nm) at the peak enhancement wavelength (indicated by the arrow in Figure 3a). An angular divergence of ≈3° is obtained along the k_x direction by measuring the full width at half maximum (FWHM) of the angular emission profile.

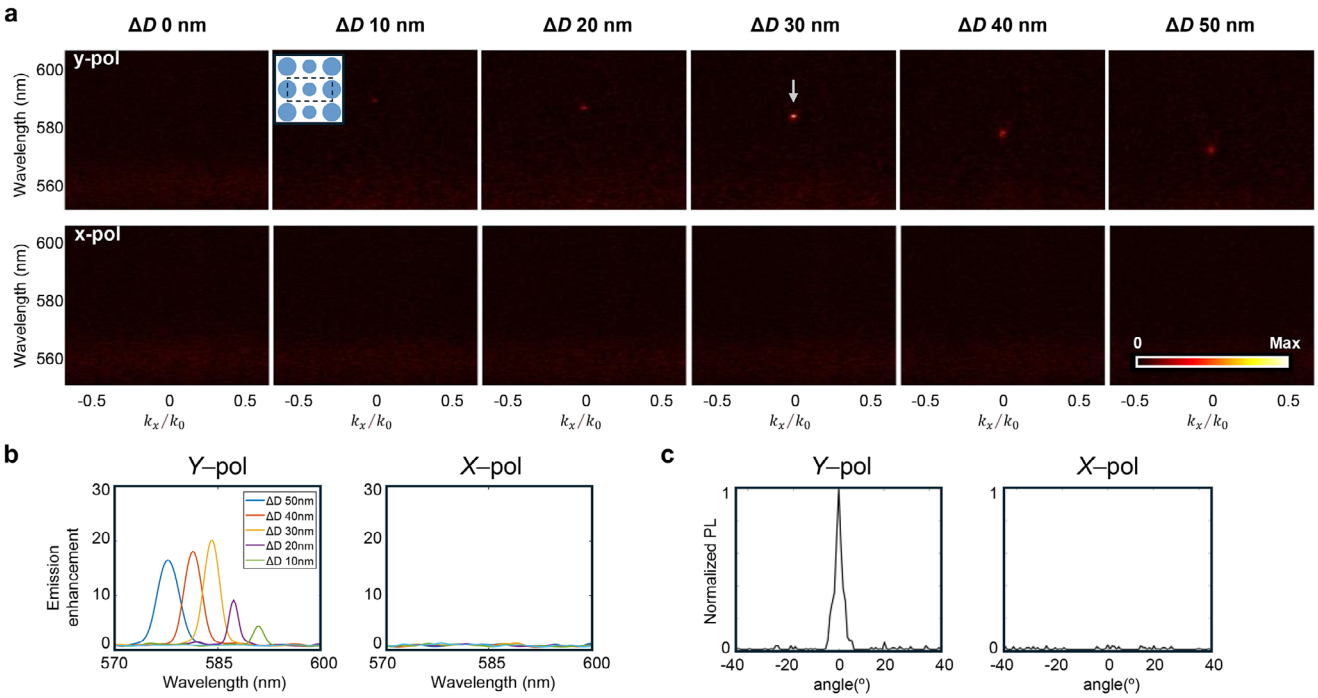

Figure 3. Experimental PL spectrum for the single-directional perturbation. a) Angle-resolved PL spectra for different ΔD values (ΔD = 0–50 nm). The upper and lower panels show the spectra for *y*- and *x*-polarized PL as a function of normalized in-plane wavevector ($k_x/k_0 = \sin\theta$, where θ is an emission angle) and wavelength. b) Emission enhancement factor and c) Angular distribution for *y*- and *x*-polarized PL in the normal direction ($k_x = 0$). An angular divergence of ≈3° is obtained for *y*-polarized PL.

Figure S16 (Supporting Information) shows the angle-resolved PL spectra along the k_y direction, which manifests the band dispersions only in the *y*-polarized PL spectra. As expected from the reciprocity calculations (Figures S12–S14, Supporting Information), the emission is more extended along the k_y direction because the perturbation is present only in the *x* direction.

Similar angle-resolved PL spectra were measured for the bidirectional perturbation (**Figure 4**). This time, all six polarization components were measured separately with varying disk sizes (ΔD = 0–70 nm). In agreement with the field enhancement calculations (Figure 2d), the maximized PL intensity is obtained for ΔD = 40 nm in the GMR position for all six polarizations (indicated by the arrows). The QD PL intensity is the most strongly enhanced in the normal direction for all six polarization components. Therefore, we experimentally observed strongly enhanced, highly directional QD emission. **Figure 5** shows the emission enhancement factors in the normal direction for the six polarization components, which are again obtained by normalizing to the PL spectrum at ΔD = 0. The maximized enhancement is achieved at ΔD = 40 nm for all six polarization components. Moreover, the experimental data exhibit almost the same emission enhancement factors (≈20 times) for the six polarization components. Therefore, the enhancement of unpolarized emission is experimentally achieved. By integrating the PL in the shaded region (corresponding to the emission band) for each polarization component, the normalized Stokes parameters of the QD emission are determined from the experimental data at ΔD = 40 nm: S_1/S_0 = 0.01, S_2/S_0 = 0.03, and S_3/S_0 = 0.01. All three normalized Stokes parameters are maintained very small, confirming unpolarized emission. The experimental data demonstrate a large enhancement in unpolarized emission via polarization-insensitive critical coupling in the BZF metasurface.

Directional light sources with polarized and unpolarized emissions can be important for AR display technology. Microdisplays and grating-based waveguide components are used in AR displays to project and overlay images on natural scenes. However, direct optical coupling into diffractive optical components from conventional light sources with a large angular divergence often suffers from very low efficiency.[45,46] Directional light sources with small divergence angles can be used to improve the coupling efficiency without a bulky collimator, enabling highly compact and ultrathin optical components for AR displays. Moreover, directional light sources can significantly increase the emission intensity in the target direction, which is highly desirable for AR displays because computer-generated images should be overlaid with bright natural background scenes.

In the current study, we demonstrated how to maximize the field enhancement by adjusting the perturbation strength in BZF metasurfaces. The field enhancement (or, equivalently, the emission enhancement by reciprocity) reaches a maximum at the critical coupling condition ($Q_{rad} = Q_{nr}$) for the given nonradiative losses. At this critical coupling condition, the maximum field enhancement becomes $I_{max} \propto 1/\gamma_{nr}$, that is, the achievable maximum field enhancement is ultimately limited by the nonradiative damping rate. Nonradiative losses can be caused by material absorption at the emission wavelength as well as random scattering due to surface roughness and lateral energy leakage due to the finite pattern size. Therefore, the achievable maximum field enhancement can be further increased in more ideal systems with lower absorption losses and reduced energy losses due to surface

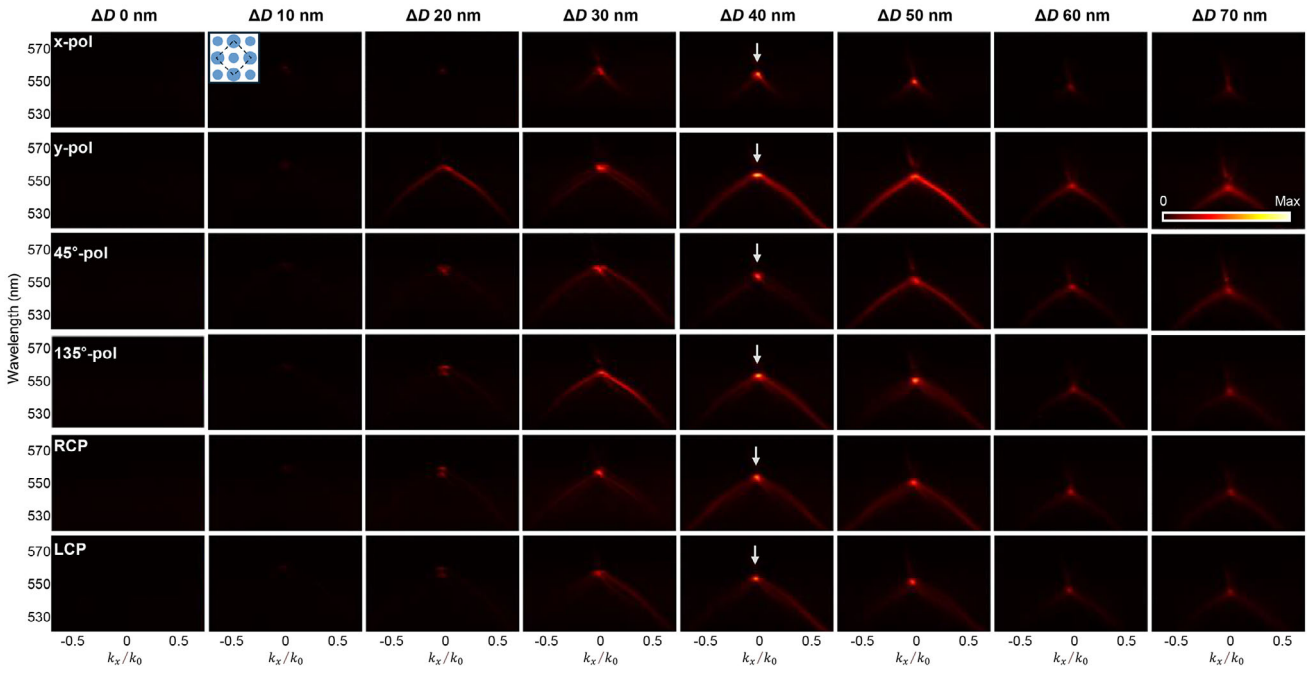

Figure 4. Experimental PL spectrum for the bidirectional perturbation. a) Angle-resolved PL spectra for different ΔD values ($\Delta D = 0$–70 nm). Each row corresponds to a different polarization component of PL. These six polarization components determine the complete polarization state (i.e., Stokes parameters) of QD emission.

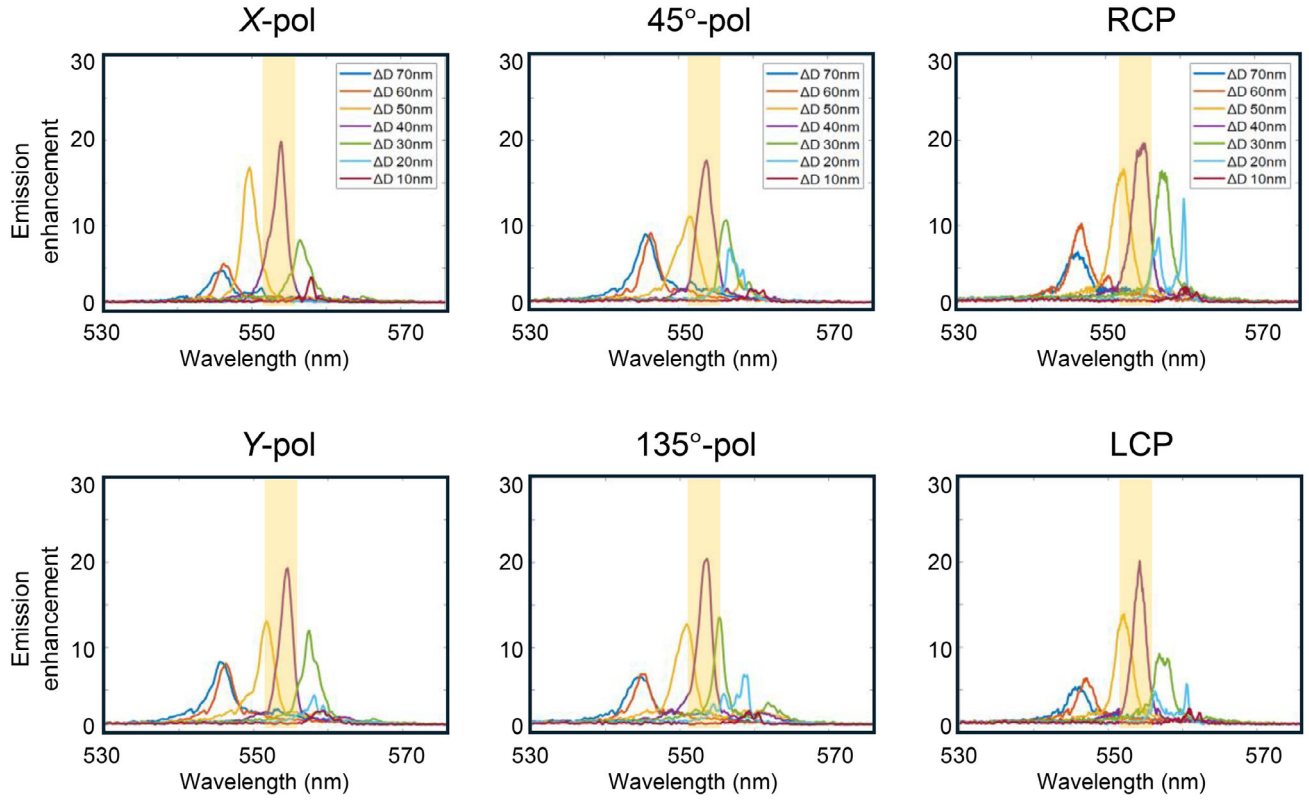

Figure 5. Emission enhancement factor for the bidirectional perturbation. Emission enhancement factors in the normal direction ($k_x = 0$) are shown for six polarization components. The six polarization components of the QD emission exhibit almost the same enhancement. By integrating the PL in the shaded region (551–555 nm) for $\Delta D = 40$ nm, the Stokes parameters are calculated from the experimental data: $S_1/S_0 = 0.01$, $S_2/S_0 = 0.03$, $S_3/S_0 = 0.01$. This confirms a large enhancement of unpolarized emission via polarization-insensitive critical coupling.

roughness and lateral leakage. For such low-loss systems, higher-Q optical modes (such as quasi-BICs) in BZF metasurfaces can be used to achieve critical coupling with reduced nonradiative losses. The concept of critical coupling can also be extended to other wave-matter interaction systems such as acoustic and elastic waves.[55–58] Therefore, it would be interesting to further extend the concept of critical coupling in BZF metasurfaces to other wave systems to maximize wave–matter interactions.

3. Conclusion

In summary, we presented a clear experimental demonstration of maximized emission enhancement at the critical coupling condition. Dielectric metasurfaces were coated with semiconductor QDs, and BZF-induced GMRs were used to gradually control the radiative Q factor and achieve critical coupling by varying the disk size. In the experiments, we clearly demonstrated the maximized enhancement of polarized and unpolarized emissions in the normal direction, leading to highly enhanced, directional, and narrow-angled QD emission. Directional light sources with polarized and unpolarized emissions and highly enhanced emission intensities can be potentially important for advanced display technologies. This study demonstrates that BZF metasurfaces can provide a highly tunable platform for both polarization-sensitive and polarization-insensitive critical coupling. The critical coupling demonstrated in this study can be readily scaled to other frequency regions, such as the infrared and terahertz ranges. Maximized field enhancement and highly enhanced light-matter interactions are important for a wide range of photonic technologies such as light sources, photodetectors, sensors, nonlinear enhancement, and quantum photonic devices.

4. Experimental Section

Sample Fabrication: 120 and 130 nm thick TiO_2 films were deposited on a transparent quartz substrate using RF sputtering. An electron beam resist (AR-P 6200.09) was spin-coated on top of the TiO_2 film, followed by the spin-coating of a conductive polymer (DisCharge DI) to reduce the charging effect. Arrays of square lattices of disk patterns (60 × 60 μm each in size) were created with varying disk sizes on the resist layer via electron beam lithography. Subsequently, a thin Cr hard mask was deposited on the substrate using an electron beam evaporator, followed by resist lift-off. Subsequently, inductively coupled plasma reactive-ion etching was performed using Ar, HBr, and BCl_3 gas mixtures. Finally, the Cr hard mask was removed using a Cr etchant (Sigma–Aldrich). CdSe/ZnS QDs (PlasmaChem) with a central emission wavelength of 540 nm were coated onto the metasurface sample with a solution concentration of 1 mg mL^{-1} in chloroform, followed by washing with isopropyl alcohol.

Optical Characterization: The angle-resolved reflectance and PL spectra were measured using a custom-built Fourier plane setup.[59,60] The back focal plane of the microscope objective was imaged, and the angle-resolved spectra were measured using a monochromator slit as the line aperture in the Fourier plane (Figure S15, Supporting Information). For reflectance spectrum measurements, a collimated white-light beam was focused on the sample surface using a high-NA microscope objective (NA: 0.75), and the intensity of the reflected beam was measured. The measured raw reflectance spectrum was normalized to the background reflectance of a smooth silver film. To measure the PL spectrum, a linearly polarized diode laser at 450 nm was used as the excitation light source (laser power: 10 μW, integration time: 5 s). The circular polarization component of the QD emission was measured using a linear polarizer and a quarter waveplate. All the measurements were conducted at room temperature.

Numerical Simulations: The band structures and Q factor calculations (in Figures 1; Figure S1, Supporting Information) were conducted using *legume* software, which implemented the guided-mode expansion method for patterned multilayer waveguides and photonic crystal slabs.[49,50] The current version of the *legume* allows for the simulation of only non-dispersive materials with constant refractive indices. Except for the band structure calculations, all numerical simulations in this study, including field enhancement and reflectance spectra, were performed using RCWA.[51]

Supporting Information

Supporting Information is available from the Wiley Online Library or from the author.

Acknowledgements

The authors acknowledge the support from the National Research Foundation (NRF) of Korea (2023R1A2C1004674 and 2022M3H4A1A04096465). This research was partially supported by the Korea Institute for Advancement of Technology (KIAT) grant funded by the Korea Government (MOTIE) (P0023703, HRD Program for Industrial Innovation).

Conflict of Interest

The authors declare no conflict of interest.

Data Availability Statement

The data that support the findings of this study are available from the corresponding author upon reasonable request.

Keywords

directional light sources, critical coupling, brillouin zone folding metasurfaces, quantum dot emission, lorentz reciprocity principle

Received: November 12, 2024
Revised: January 14, 2025
Published online:

[1] A. Yariv, *IEEE Photonics Technol. Lett.* **2002**, *14*, 483.
[2] J. R. Tischler, M. S. Bradley, V. Bulović, *Opt. Lett.* **2006**, *31*, 2045.
[3] B. Neuner III, D. Korobkin, C. Fietz, D. Carole, G. Ferro, G. Shvets, *Opt. Lett.* **2009**, *34*, 2667.
[4] M. A. Kats, D. Sharma, J. Lin, P. Genevet, R. Blanchard, Z. Yang, M. M. Qazilbash, D. Basov, S. Ramanathan, F. Capasso, *Appl. Phys. Lett.* **2012**, *101*, 221101.
[5] J. Park, J.-H. Kang, A. P. Vasudev, D. T. Schoen, H. Kim, E. Hasman, M. L. Brongersma, *ACS Photonics* **2014**, *1*, 812.
[6] Y. Ra'di, A. Krasnok, A. Alú, *ACS Photonics* **2020**, *7*, 1468.
[7] K. Koshelev, Y. Tang, Z. Hu, I. I. Kravchenko, G. Li, Y. Kivshar, *ACS Photonics* **2023**, *10*, 298.
[8] J. Wang, T. Weber, A. Aigner, S. A. Maier, A. Tittl, *Laser Photonics Rev.* **2023**, *17*, 2300294.
[9] M. S. Ergoktas, A. Kecebas, K. Despotelis, S. Soleymani, G. Bakan, A. Kocabas, A. Principi, S. Rotter, S. K. Ozdemir, C. Kocabas, *Science* **2024**, *384*, 1122.

[10] C. Schiattarella, S. Romano, L. Sirleto, V. Mocella, I. Rendina, V. Lanzio, F. Riminucci, A. Schwartzberg, S. Cabrini, J. Chen, L. Liang, X. Liu, G. Zito, *Nature* **2024**, *626*, 765.
[11] J. Hinney, S. Kim, G. J. Flatt, I. Datta, A. Alù, M. Lipson, *Nat. Commun.* **2024**, *15*, 2741.
[12] T. J. Seok, A. Jamshidi, M. Kim, S. Dhuey, A. Lakhani, H. Choo, P. J. Schuck, S. Cabrini, A. M. Schwartzberg, J. Bokor, E. Yablonovitch, M. C. Wu, *Nano Lett.* **2011**, *11*, 2606.
[13] N. Bernhardt, K. Koshelev, S. J. White, K. W. C. Meng, J. E. Froch, S. Kim, T. T. Tran, D.-Y. Choi, Y. Kivshar, A. S. Solntsev, *Nano Lett.* **2020**, *20*, 5309.
[14] A. Vaskin, R. Kolkowski, A. F. Koenderink, I. Staude, *Nanophotonics* **2019**, *8*, 1151.
[15] I. Staude, T. Pertsch, Y. S. Kivshar, *ACS Photonics* **2019**, *6*, 802.
[16] S. Yuan, X. Qiu, C. Cui, L. Zhu, Y. Wang, Y. Li, J. Song, Q. Huang, J. Xia, *ACS Nano* **2017**, *11*, 10704.
[17] S. Liu, A. Vaskin, S. Addamane, B. Leung, M.-C. Tsai, Y. Yang, P. P. Vabishchevich, G. A. Keeler, G. Wang, X. He, Y. Kim, N. F. Hartmann, H. Htoon, S. K. Doorn, M. Zilk, T. Pertsch, G. Balakrishnan, M. B. Sinclair, I. Staude, I. Brener, *Nano Lett.* **2018**, *18*, 6906.
[18] S. Murai, G. W. Castellanos, T. Raziman, A. G. Curto, J. G. Rivas, *Adv. Opt. Mater.* **2020**, *8*, 1902024.
[19] L. Zhu, S. Yuan, C. Zeng, J. Xia, *Adv. Opt. Mater.* **2020**, *8*, 1901830.
[20] Z. Zhang, C. Xu, C. Liu, M. Lang, Y. Zhang, M. Li, W. Lu, Z. Chen, C. Wang, S. Wang, X. Li, *Nano Lett.* **2023**, *23*, 7584.
[21] E. Csányi, Y. Liu, S. D. Rezaei, H. Y. L. Lee, F. Tjiptoharsono, Z. Mahfoud, S. Gorelik, X. Zhao, L. J. Lim, D. Zhu, J. Wu, K. E. J. Goh, W. Gao, Z.-K. Tan, G. Leggett, C.-W. Qiu, Z. Dong, *Adv. Funct. Mater.* **2024**, *34*, 2309539.
[22] S. C. An, Y. Lim, K. Y. Lee, D. Choi, S. Kim, S. H. Gong, J. W. Yoon, Y. C. Jun, *Adv. Funct. Mater.* **2024**, *34*, 2313840.
[23] Y. Mohtashami, R. A. DeCrescent, L. K. Heki, P. P. Iyer, N. A. Butakov, M. S. Wong, A. Alhassan, W. J. Mitchell, S. Nakamura, S. P. DenBaars, J. A. Schuller, *Nat. Commun.* **2021**, *12*, 3591.
[24] S. Kim, B. H. Woo, S.-C. An, Y. Lim, I. C. Seo, D.-S. Kim, S. Yoo, Q.-H. Park, Y. C. Jun, *Nano Lett.* **2021**, *21*, 10076.
[25] X. Zhang, Y. Liu, J. Han, Y. Kivshar, Q. Song, *Science* **2022**, *377*, 1215.
[26] Y. Lim, I. C. Seo, S. C. An, Y. Kim, C. Park, B. H. Woo, S. Kim, H. R. Park, Y. C. Jun, *Laser Photonics Rev.* **2023**, *17*, 2200611.
[27] S. Kim, S.-C. An, Y. Kim, Y. S. Shin, A. A. Antonov, I. C. Seo, B. H. Woo, Y. Lim, M. V. Gorkunov, Y. S. Kivshar, J. Y. Kim, Y. C. Jun, *Sci. Adv.* **2023**, *9*, eadh0414.
[28] Y. Sun, Z. Hu, K. Shi, T. Guo, Y. Xing, Y. Jin, S. He, *Adv. Opt. Mater.* **2023**, *11*, 2300197.
[29] M. Xia, Y. Chen, J. Zhou, Y. Wang, D. Huang, X. Zhang, *Adv. Mater.* **2024**, *36*, 2400214.
[30] M. Jeong, B. Ko, C. Jung, J. Kim, J. Jang, J. Mun, J. Lee, S. Yun, S. Kim, J. Rho, *Nano Lett.* **2024**, *24*, 5783.
[31] M. Ramezani, G. Lozano, M. A. Verschuuren, J. Gómez-Rivas, *Phys. Rev. B* **2016**, *94*, 125406.
[32] S. Zhang, E. R. Martins, A. G. Diyaf, J. I. Wilson, G. A. Turnbull, I. D. Samuel, *Synth. Met.* **2015**, *205*, 127.
[33] C. W. Neff, T. Yamashita, C. J. Summers, *Appl. Phys. Lett.* **2007**, *90*, 021102.
[34] A. C. Overvig, S. Shrestha, N. Yu, *Nanophotonics* **2018**, *7*, 1157.
[35] A. C. Overvig, S. C. Malek, M. J. Carter, S. Shrestha, N. Yu, *Phys. Rev. B* **2020**, *102*, 035434.
[36] P. Vaity, H. Gupta, A. Kala, S. D. Gupta, Y. S. Kivshar, V. R. Tuz, V. G. Achanta, *Adv. Photonics Res.* **2022**, *3*, 2100144.
[37] S. Murai, D. R. Abujetas, L. Liu, G. W. Castellanos, V. Giannini, J. A. Sánchez-Gil, K. Tanaka, J. G. Rivas, *Laser Photonics Rev.* **2022**, *16*, 2100661.
[38] W. Wang, Y. K. Srivastava, T. C. Tan, Z. Wang, R. Singh, *Nat. Commun.* **2023**, *14*, 2811.
[39] A. C. Overvig, M. Cotrufo, M. Markowitz, Y. Zhou, B. Hao, K. Stensvad, C. Schardt, A. Alù, *ACS Photonics* **2023**, *10*, 1832.
[40] X. F. Yan, Y. J. Xie, S. Chen, P. Y. Wu, *Adv. Opt. Mater.* **2024**, *12*, 2401027.
[41] K. Sun, W. Wang, Z. Han, *Phys. Rev. B.* **2024**, *109*, 085426.
[42] J. Zhou, M. Xia, Y. Chen, X. Zhang, *ACS Photonics* **2024**, *11*, 2707.
[43] H. Zhong, L. Huang, S. Li, C. Zhou, S. You, L. Li, Y. Cheng, A. E. Miroshnichenko, *Appl. Phys. Rev.* **2024**, *11*, 031404.
[44] W. Adi, S. Rosas, A. Beisenova, S. K. Biswas, H. Mei, D. A. Czaplewski, F. Yesilkoy, *Nat. Commun.* **2024**, *15*, 10049.
[45] X. Fu, Y. Mehta, Y. A. Chen, L. Lei, L. Zhu, N. Barange, Q. Dong, S. Yin, J. Mendes, S. He, R. Gogusetti, C.-H. Chang, F. So, *Adv. Mater.* **2021**, *33*, 2006801.
[46] Y.-H. Lee, T. Zhan, S.-T. Wu, *Virtual Real. Intell. Hardw.* **2019**, *1*, 10.
[47] T. Zhan, K. Yin, J. Xiong, Z. He, S.-T. Wu, *iscience* **2020**, *23*, 101397.
[48] Z. Liu, D. Wang, H. Gao, M. Li, H. Zhou, C. Zhang, *Advanced Photonics* **2023**, *5*, 034001.
[49] M. Minkov, I. A. Williamson, L. C. Andreani, D. Gerace, B. Lou, A. Y. Song, T. W. Hughes, S. Fan, *ACS Photonics* **2020**, *7*, 1729.
[50] S. Zanotti, M. Minkov, D. Nigro, D. Gerace, S. Fan, L. C. Andreani, *Comput. Phys. Commun.* **2024**, *304*, 109286.
[51] J. P. Hugonin, P. Lalanne, arXiv **2021**, arXiv, 2101.00901.
[52] L. Novotny, B. Hecht, *Principles of nano-optics*, Cambridge University Press, UK **2012**.
[53] K. Sun, H. Wei, W. Chen, Y. Chen, Y. Cai, C.-W. Qiu, Z. Han, *Phys. Rev. B.* **2023**, *107*, 115415.
[54] K. Sun, Y. Cai, U. Levy, Z. Han, *Beilstein J. Nanotechnol.* **2023**, *14*, 322.
[55] H. Long, Y. Cheng, J. Tao, X. Liu, *Appl. Phys. Lett.* **2017**, *110*, 023502.
[56] S.-Y. Yu, C. He, X.-C. Sun, H.-F. Wang, J.-Q. Wang, Z.-D. Zhang, B.-Y. Xie, Y. Tian, M.-H. Lu, Y.-F. Chen, *Natl. Sci. Rev.* **2021**, *8*, nwaa262.
[57] X. Li, Z. Yu, H. Iizuka, T. Lee, *Extreme Mech. Lett.* **2022**, *52*, 101649.
[58] X. Yu, Y. Mi, W. Zhai, L. Cheng, *J. Acoust. Soc. Am.* **2023**, *154*, 2988.
[59] I. C. Seo, S. Kim, B. H. Woo, I.-S. Chung, Y. C. Jun, *Nanophotonics* **2020**, *9*, 4565.
[60] Y. Zhang, M. Zhao, J. Wang, W. Liu, B. Wang, S. Hu, G. Lu, A. Chen, J. Cui, W. Zhang, C. W. Hsu, X. Liu, L. Shi, H. Yin, J. Zi, *Sci. Bull.* **2021**, *66*, 824.